INTERNATIONAL JOURNAL FOR NUMERICAL METHODS IN FLUIDS
Int. J. Numer. Meth. Fluids 2000; **32**: 515–543

A particle-in-cell method for the solution of two-layer shallow-water equations

Benoit Cushman-Roisin[a,*], Oleg E. Esenkov[b] and Benedict J. Mathias[c]

[a] *Thayer School of Engineering, Dartmouth College, Hanover, NH 03755-8000, U.S.A.*
[b] *Rosenstiel School of Marine and Atmospheric Science, University of Miami, Miami, FL 33149-1098, U.S.A.*
[c] *i2 Technologies, 303 Twin Dolphin Drive, Redwood City, CA 94065, U.S.A.*

SUMMARY

A particle-in-cell (PIC) numerical method developed for the study of shallow-water dynamics, when the moving fluid layer is laterally confined by the intersection of its top and bottom surfaces, is described. The effect of ambient rotation is included for application to geophysical fluids, particularly open-ocean buoyant vortices in which the underlying density interface outcrops to the surface around the rim of the vortex. Extensions to include the dynamical effect of a second moving layer (baroclinicity) and the presence of a lateral rigid boundary (sidewall) are also described. Although the method was developed for oceanographic investigations, applications to other fluid mechanics problems would be straightforward.

KEY WORDS: open-ocean; particle-in-cell; shallow-water equation

1. INTRODUCTION

There are a number of situations, mostly geophysical in nature, where fluid flows occur in layers that are much thinner than they are wide. In such cases, hydrostatic equilibrium is invoked in the vertical, and the equations of motion reduce to the so-called St. Venant or shallow-water equations [1]. Horizontal velocity components (say u and v) are taken as uniform in the vertical, across a layer of thickness (say h) extending from a lower surface (which may be a solid bottom or the top of another denser fluid layer) to an upper surface (which may be a free surface, if the fluid is a liquid, or the base of an overlying buoyant fluid layer). Particular cases of interest here are those when the layer terminates at an edge somewhere, such as in the dam-breaking problem, where the free surface reaches the bottom at the head of the advancing bore. Another case of importance in oceanography is that of large open-ocean vortices consisting of a buoyant layer in rotation while floating atop denser

* Correspondence to: Thayer School of Engineering, Dartmouth College, 8000 Cummings Hall, Hanover, NH 03755-8000, U.S.A.

CCC 0271–2091/2000/050515–29$17.50

Received 18 February 1998
Revised 14 January 1999

seawater; in that case, the density interface (called pycnocline) separating the buoyant vortex from the underlying ocean water reaches the sea surface along the perimeter of the vortex, thereby encircling a finite volume of buoyant water moving within a deformable rim (Figure 1).

The vanishing of the layer thickness at a moving point (in one-dimensional form) or along a distorting line (in two-dimensional form) creates severe problems for the numerical modeler. With a fixed grid, the number of wet points (where $h > 0$) varies over time, and the tracking, particularly in two-dimensional form, of the edge line (where $h = 0$) between grid points, requires extreme care to avoid undue numerical diffusion and/or instabilities. Methods specifically developed for free-surface problems, such as the height–function method [2], the volume-of-fluid method [3] and the marker–particle method [4], could be adapted by tipping the geometry sideways (the upper free surface becoming the lateral edge line). Although these methods have their respective virtues, they are essentially Eulerian methods with disparate treatment given to grid points in the vicinity of the edge.

An alternative approach, which takes greater advantage of the fact that the motion of the edge follows fluid–particle motion, is the semi-Lagrangian method of particles in cell. Originally developed for fluid dynamics problems with contact discontinuities, such as those

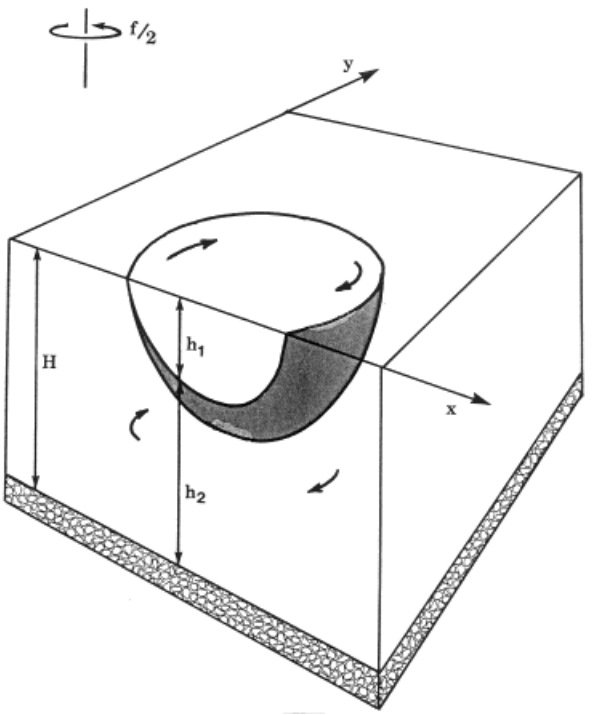

Figure 1. Sketch of a lens-like vortex in a two-layer shallow-water system, with attending notation.

with shocks and free surfaces, the particle-in-cell (PIC) method [5,6] has found wide applications in plasma physics and astrophysics. It was later adapted to single-layer shallow-water dynamics with an edge [7–9]. The method essentially combines Lagrangian and Eulerian descriptions, treating each part of the model by the approach that fits it best. In shallow-water applications, the field variables, such as pressure and layer thickness, are evaluated on a fixed Eulerian mesh (defining the cells), while the variables that are naturally attached to fluid particles, such as velocities, accelerations and forces, are calculated using a Lagrangian description.

Point–vortex methods have enjoyed a certain popularity in two-dimensional fluid mechanics [10] and geophysical fluid dynamics [11; and references therein]. One should, however, not confuse those methods with typical PIC methods, such as the one presented here. The essential difference is that vortex methods track particles that conserve their circulation (horizontally integrated vorticity), while the present PIC method tracks particles that conserve their individual volume (horizontally integrated layer thickness). Consequently, vortex methods *integrate* vorticity to obtain velocity (usually via a streamfunction), while PIC methods *differentiate* a pressure field to obtain the velocities (via accelerations). Also, vortex methods rely on a linear relationship between vorticity and velocity, which can be lost in geophysical applications when potential vorticity supersedes regular vorticity; in contrast, the present PIC method does not have such a handicap and is therefore much more flexible.

The chief advantage of the PIC method is its total avoidance of tracking the edge–line distortion over time. In the model, the edge is simply the envelope of the group (or groups) of particles, which is easily perceived by the eye upon examination of a plot, but never needs to be constructed by the computer code. A critical procedure in the model is the transfer, at least once each way per time step, of information between the set of particles and the mesh defining the cells. Particle information is mapped onto the mesh by tallying characteristics of the particles in every cell. For example, the volume of fluid in a cell is equal to the sum of the volumes of the particles in that cell, and subsequent division by the cell area yields the fluid thickness. In reverse, grided information is transferred to particles by interpolation. For example, pressure gradient forces previously calculated at grid points are interpolated to particle sites before marching the particles forward in time. These particle–grid transfers are critical to the performance of the method, and their implementation demands that care be given to accuracy and stability. A certain degree of smoothing is necessary in order that the contribution of a particle passing from one cell to an adjacent cell be gradually removed from the cell of origin and gradually provided to the receiving cell. Insufficient smoothing would create undesirable fluctuations whenever a particle changes cell, while too much smoothing would cause excessive diffusion. Also, attention needs to be paid to the average number of particles per cell; too few leads to computational noise, while too many leads to computational waste.

The PIC method handles moving edges with great ease, but encounters difficulties in the presence of solid boundaries. This is because particle velocities are calculated from accelerations, which are derived from the forces acting on them, and there is therefore no immediate way of setting a velocity component to zero at a boundary. The knowledge of the proximity of a boundary can only be imparted to particles in some indirect way. While there may be several ways to accomplish this, we propose here a reflection method that returns particles

having crossed the boundary back into the fluid domain with due attention paid to conservation of the appropriate form of linear momentum and of kinetic energy.

The purpose of the present article is to describe a PIC method for the two-layer shallow-water system, first in a doubly periodic domain and then in the presence of a straight solid boundary. The underlying dynamical framework includes the Coriolis force and neglects explicit forms of dissipation (because of our interest in geophysical fluid applications). Each version of the model is tested and evaluated in situations of oceanographic interest.

2. THE MATHEMATICAL MODEL

2.1. Two-layer shallow-water equations

We consider a two-layer system of inviscid and incompressible fluid with constant densities ρ_1 and ρ_2 on a flat bottom (Figure 1). (Extension to irregular bottom topography is trivial.) The shallow-water equations that describe the motion of such system are

$$\frac{\partial u_i}{\partial t} + u_i \frac{\partial u_i}{\partial x} + v_i \frac{\partial u_i}{\partial y} - f v_i = -\frac{1}{\rho_0} \frac{\partial p_i}{\partial x} \tag{1}$$

$$\frac{\partial v_i}{\partial t} + u_i \frac{\partial v_i}{\partial x} + v_i \frac{\partial v_i}{\partial y} + f u_i = -\frac{1}{\rho_0} \frac{\partial p_i}{\partial y} \tag{2}$$

$$\frac{\partial h_i}{\partial t} + \frac{\partial (h_i u_i)}{\partial x} + \frac{\partial (h_i v_i)}{\partial y} = 0 \tag{3}$$

where the subscript $i = 1, 2$ indicates the upper and lower layer respectively; p_i, h_i and (u_i, v_i) are the pressure, thickness and velocity components in each layer. The coefficient f, the Coriolis parameter due to ambient rotation (such as Earth's rotation), may in general be a function of the horizontal co-ordinates (x, y) but will be taken as a positive constant here.

This set of equations is completed by a geometric relation and the hydrostatic balance

$$h_1 + h_2 = H \tag{4}$$

$$p_1 = p_2 + \rho_0 g' h_1 \tag{5}$$

In these last equations, H is the total depth of the fluid and g' is the reduced gravity $[g' = g(\rho_2 - \rho_1)/\rho_2]$. Because the free-surface vertical elevations are much smaller than those of the interface separating the two layers, we can use the rigid-lid approximation, which eliminates surface gravity waves but preserves internal gravity waves (interfacial waves). Furthermore, if we assume a flat bottom, the total depth H is constant.

We allow the upper layer to terminate ($h_1 = 0$) within the fluid domain. Beyond such line(s), only the lower layer exists, and the set of equations reduces to the lower-layer equations [(1)–(3) with $i = 2$ only and $h_2 = H$]. The lower layer is assumed to exist throughout the intregration domain ($h_2 > 0$ everywhere and at all times).

2.2. Non-dimensionalization and simplification

As shown by Mathias [12], these equations can be non-dimensionalized using a single external scale. Taking h_1 as the scale for the upper-layer thickness (such as the maximum value of h_1 at the initial time), we can form the scales $U = \sqrt{g'H_1}$ for all velocity components, $L = U/f = \sqrt{g'H_1}/f$ for the spatial co-ordinates, $P = \rho_0 g' H_1$ for the pressures, and $L/U = 1/f$ for time. If the total depth H is much larger than the upper-layer thickness ($H \gg H_1$), the equations can be further reduced to the following, lower-order set [12]:

$$\frac{\partial u_1}{\partial t} + u_1 \frac{\partial u_1}{\partial x} + v_1 \frac{\partial u_1}{\partial y} - v_1 = -\frac{\partial (p_2 + h_1)}{\partial x} \tag{6}$$

$$\frac{\partial v_1}{\partial t} + u_1 \frac{\partial v_1}{\partial x} + v_1 \frac{\partial v_1}{\partial y} + u_1 = -\frac{\partial (p_2 + h_1)}{\partial y} \tag{7}$$

$$\frac{\partial h_i}{\partial t} + \frac{\partial (h_1 u_1)}{\partial x} + \frac{\partial (h_1 v_1)}{\partial y} = 0 \tag{8}$$

$$q_2 = \nabla^2 p_2 + \delta h_1 \tag{9}$$

$$\frac{\partial q_2}{\partial t} + J(p_2, q_2) = 0 \tag{10}$$

where q_2 is the so-called potential vorticity (of the lower layer), $\delta = H_1/H$ is a constant parameter, and $J(a, b) = (\partial a/\partial x)(\partial b/\partial y) - (\partial a/\partial y)(\partial b/\partial x)$ is the Jacobian operator. In regions beyond the termination of the upper layer, the set of equations reduces to Equations (9) and (10) with $h_1 = 0$, which are the two-dimensional Euler equations in vorticity form. The single-layer system is obtained in the limit $\delta = p_2 = q_2 = 0$. If the lower layer is active ($\delta > 0$), the q_2 field must be specified at the initial time. Note that, although q_2 may be taken as zero initially, and therefore remain so at all times, the accompanying pressure p_2 will generally not be zero, and the lower layer will be in motion, thereby excercizing an influence on the upper layer.

Because the lower layer extends throughout the integration domain, its equations (9) and (10) can be solved with a conventional finite difference or spectral method. One of our objectives is to show how a PIC representation for one layer (layer 1 here) can be coupled to a traditional scheme for another dynamically active layer (layer 2 here), but the actual nature of the dynamics in that another layer is not of particular interest. Therefore, the dynamical simplification performed on the lower layer (called quasi-geostrophic approximation in the jargon of meteorology and oceanography) has no significant importance here.

2.3. Invariants

The governing equations (6)–(10) possess global invariants under certain boundary conditions. For systems with an upper layer entirely contained within one or several outcrops (lines of $h_1 = 0$) and with p_2 vanishing at large distances outside of these outcrops, the invariants are

Upper layer volume:

$$V = \int\int h_1 \, \mathrm{d}x \, \mathrm{d}y \tag{11}$$

Total angular momentum:

$$A = \int\int \left[h_1(xv_1 - yu_1) + \frac{1}{\delta}\left(x\frac{\partial p_2}{\partial x} + y\frac{\partial p_2}{\partial y} \right) \right] \mathrm{d}x \, \mathrm{d}y \tag{12}$$

Total energy:

$$E = \int\int \left[\frac{1}{2} h_1(u_1^2 + v_1^2) + \frac{1}{2} h_1^2 + \frac{1}{2\delta} |\nabla p_2|^2 \right] \mathrm{d}x \, \mathrm{d}y \tag{13}$$

Any function of the upper layer potential vorticity:

$$C = \int\int \left[\frac{1}{h_1}\left(1 + \frac{\partial v_1}{\partial x} - \frac{\partial u_1}{\partial y} \right) \right]^m h_1 \, \mathrm{d}x \, \mathrm{d}y \tag{14}$$

Any function of the lower layer potential vorticity:

$$Z = \int\int \frac{1}{\delta} q_2^n \, \mathrm{d}x \, \mathrm{d}y \tag{15}$$

where all integrations cover the infinite (x, y) plane. In practice, the integrations can be limited to regions where the upper layer exists ($h_1 \geq 0$) and their surrounding zones, where lower layer motions are significant. The last two invariants are actually groups of invariants, for the exponents m and n can take any positive value.

3. THE NUMERICAL METHOD

To solve the upper layer equations (6)–(8), we use the PIC approach. Thus, we dissect the upper layer fluid in a large number of material particles. Particle k ($k = 1, \ldots, N$, N being the total number of particles) is assigned a volume V_k, which remains constant over time. Because all particles retain their volume, no volume is lost or gained, and the upper layer continuity equation (8) is automatically satisfied and needs no further mention.

Besides a volume, every particle is also assigned a position (x_k, y_k), a velocity (u_k, v_k) and an acceleration (a_k, b_k); all functions of time. Position is related to velocity, and velocity to acceleration according to immediate kinematic relations

$$\frac{\mathrm{d}x_k}{\mathrm{d}t} = u_k, \qquad \frac{\mathrm{d}y_k}{\mathrm{d}t} = v_k \tag{16}$$

$$\frac{\mathrm{d}u_k}{\mathrm{d}t} = a_k, \qquad \frac{\mathrm{d}v_k}{\mathrm{d}t} = b_k. \tag{17}$$

In the numerical code, the updating of both position and velocity is performed with a fourth-order Adams–Bashforth scheme [13].

The crux of the method is, of course, to relate the accelerations to the Coriolis (if present) and pressure forces, and to relate the latter to the particle positions and the activity in the lower layer. For this, we use a Eulerian square mesh, which defines the cells and which naturally coincides with the grid used to solve the lower layer equations. At the nodes of this grid, the upper layer thickness h_1, the two pressures p_1 and p_2, and the lower layer potential vorticity q_2 are computed. The calculations proceed as follows. From the particle positions (x_k, y_k), the upper layer thickness distribution is calculated as volume per area

$$h_1(x, y, t) = \sum_{k=1}^{N} V_k \delta(x - x_k)\delta(y - y_k) \tag{18}$$

where ideally $\delta(\xi)$ (of dimension equal to the inverse of a length) should be the Dirac function, but is replaced out of numerical necessity by a trapezoidal function spanning several grid nodes. We take [8]

$$\begin{aligned} \delta(\xi) &= \frac{1}{2\Delta} && \text{for } |\xi| \le \frac{\Delta}{2} \\ &= \frac{1}{2\Delta}\left(\frac{3}{2} - \frac{|\xi|}{\Delta}\right) && \text{for } \frac{\Delta}{2} \le |\xi| \le \frac{3\Delta}{2} \\ &= 0 && \text{for } \frac{3\Delta}{2} \le |\xi| \end{aligned} \tag{19}$$

where Δ is the grid size (Figure 2). Spreading over a span larger than Δ in each horizontal direction is necessary to ensure a smooth exit of a particle from $\Delta \times \Delta$ cells and its gradual entrance into one of the neighboring cells.

The next step is the determination of the pressure fields on the grid. First, the current grided values of the lower layer potential vorticity q_2 are combined with the just acquired upper layer thickness h_1 to form a grided set of $q_2 - \delta h_1$ values, from which the lower layer pressure field can be calculated via (9),

$$\nabla^2 p_2 = q_2 - \delta h_1 \tag{20}$$

We solve this Poisson equation by successive overrelaxation, but a spectral method could also be used. From p_2 the upper layer pressure follows immediately by a simple addition,

$$p_1 = p_2 + h_1 \tag{21}$$

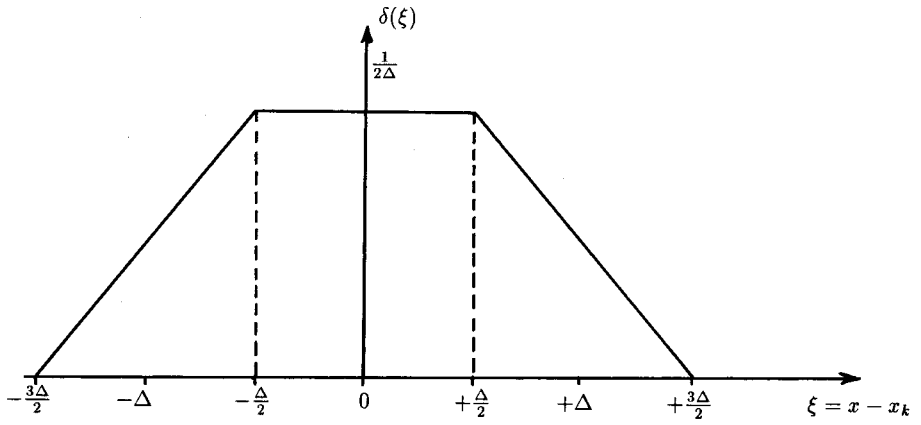

Figure 2. Trapezoidal function for the spreading of a particle contribution, such as volume, over neighboring grid nodes. Since the span of non-zero values stretches over 3Δ, three nodes receive partial contributions, in one direction. Because of the two-dimensional nature of the system, the particle contribution is actually spread over a square of nine nodes, with the center being the grid node that is the closest to the particle.

The lower layer pressure is also used to march the q_2 field in time, according to its evolution equation (10)

$$\frac{\partial q_2}{\partial t} = -J(p_2, q_2) \tag{22}$$

where the Jacobian operator is discretized on the grid according to a traditional Arakawa scheme [14] (Scheme B).

Spatial derivatives $\partial p_1/\partial x$ and $\partial p_1/\partial y$ of the upper layer pressure are calculated by centered differences at interior grid nodes of the domain and by second-order one-sided differences at points lying on boundaries, if any. Finally, this pressure gradient is interpolated from the grid to the particle locations using the identical weights as those used for the earlier transfer (18) of particle information to the grid. The pressure gradient is, within a change of sign, the pressure force. To it is added the Coriolis force (if present) to obtain the acceleration via Newton's law,

$$a_k = +v_k - \left[\frac{\partial p_1}{\partial x}\right]_k \tag{23}$$

$$b_k = -u_k - \left[\frac{\partial p_1}{\partial y}\right]_k \tag{24}$$

These last equations replace the momentum equations (6) and (7). Note that, in contrast to applications of the PIC method to plasma physics, there is no direct particle–particle interaction, only an indirect interaction through the pressure gradient.

In summary, our algorithm works as follows (Figure 3). First we distribute the particles across the domain to represent an upper layer with the desired shape (i.e. setting V_k, x_k and y_k, for $k = 1, \ldots, N$), assign velocity components to every particle (u_k and V_k, for $k = 1, \ldots, N$), and initialize the potential vorticity field of the lower layer (grided array of q_2 values). Then, we calculate the upper layer thickness h_1 at each grid point using the volume sharing technique (18). Next, we combine q_2 and h_1 and solve (20) for p_2 by successive overrelaxation (SOR). This lower layer pressure field is then used twice, the first time to form the upper layer pressure p_1 according to the hydrostatic equation (21) and again to update the lower layer potential vorticity q_2 with (22). The upper layer pressure gradient is calculated on the grid and then interpolated to the particle sites, thus providing the pressure force acting on every particle. To this pressure force is added the Coriolis force, and the acceleration is derived from Newton's Law (23) and (24) for every particle. We finally update the particle positions with the current velocities, and the velocities with the current accelerations, using (16) and (17) respectively. The procedure is repeated as often as time steps are desired.

4. VORTEX SIMULATIONS

In a first series of performance experiments, we apply our model to the study of lens-like oceanic vortices, investigating isolated circular and elliptical vortices, then the merger of two circular vortices, and finally the evolution of a circular vortex in the presence of a non-concentric circular flow in the lower layer.

To initialize particles in a vortex formation, we proceed as follows. We first fill a unit circle ($\sqrt{x^2 + y^2} = r \leq 1$) with N particles located at random, according to a uniform distribution whereby the co-ordinates of the kth particle are set from

$$x_k = r_k \cos \theta_k, \qquad y_k = r_k \sin \theta_k \tag{25a}$$

$$r_k = \sqrt{n_1}, \qquad \theta_k = 2\pi n_2 \tag{25b}$$

where (n_1, n_2) is the kth pair in a series of random numbers between 0 and 1. (The square root of n_1 forces more particles to lie at larger radii precisely to achieve a uniform distribution over the unit circle.) We then assign a volume to every particle so as to impose a parabolic thickness profile of unit center depth and vanishing thickness at unit radius [$h_1(r) = 1 - r^2,\ 0 \leq r \leq 1$]. By virtue of the random distribution, every particle is expected to occupy the same fraction π/N of the unit circle area, and the volume assigned to the kth particle is thus the product of the layer thickness at radius r_k by the horizontal area π/N that it occupies

$$V_k = \frac{\pi(1 - r_k^2)}{N} \tag{26}$$

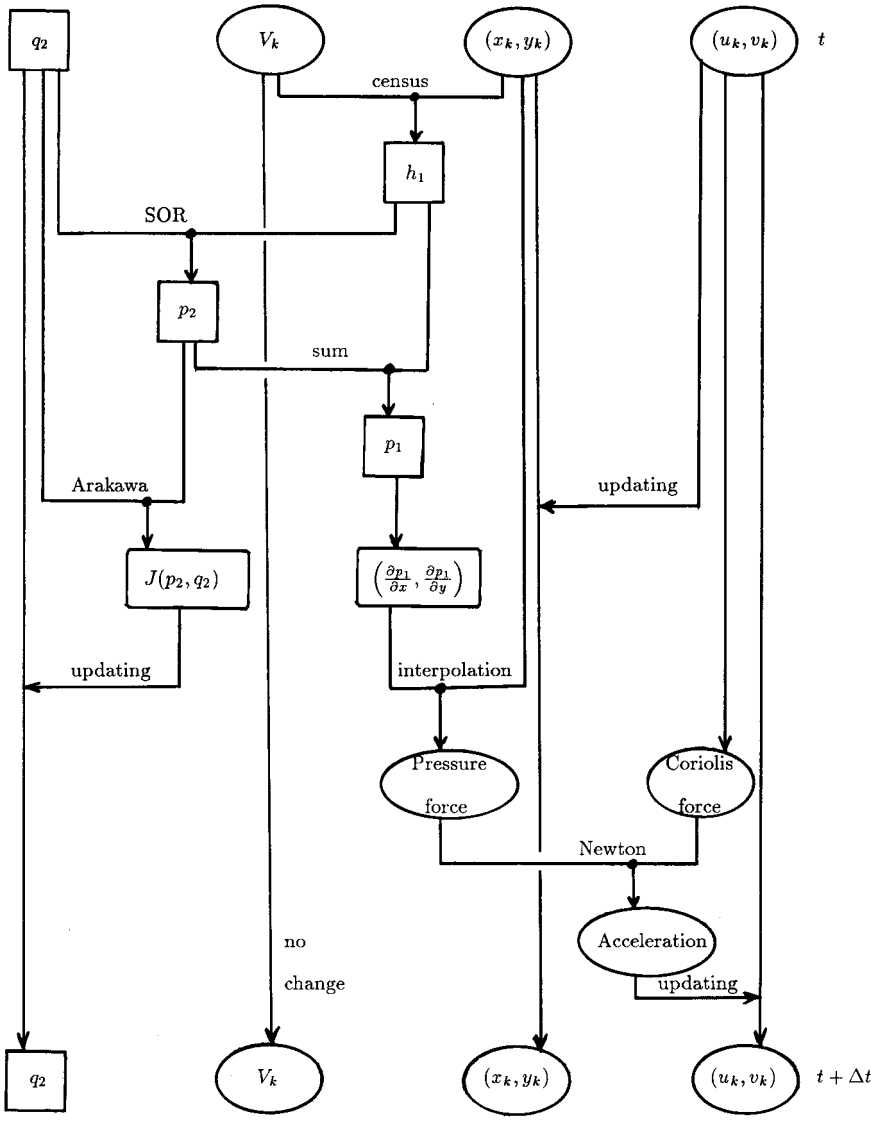

Figure 3. Hierarchy of calculations of the present PIC method. Variables in square boxes exist on the grid, while those in elliptical boxes correspond to particles. The 'census' step consists in assigning fractions of every particle's volume to a set of neighboring grid points, while the 'interpolation' step uses the same weights in reverse. All 'updating' steps use a fourth-order time stepping scheme (requiring that the hierarchy of steps be performed four times per actual time step).

The next step is to give to the vortex its actual horizontal and vertical dimensions by scaling the particle volumes and position co-ordinates appropriately. If an elliptical vortex is desired, distinct scalings are used for the x and y co-ordinates. For a central depth h_0, semi-major axis a and semi-minor axis b, i.e.

$$h_1 = h_0\left(1 - \frac{x^2}{a^2} - \frac{y^2}{b^2}\right) \tag{27}$$

all volumes are multiplied by abh_0, x co-ordinates by a, and y co-ordinates by b. Because we will restrict our attention to cases either with a single vortex or with two vortices of equal initial central thickness, we can choose the unique central thickness as the dimensional scale H_1 and consequently take $h_0 = 1$. Finally, every particle is assigned an initial velocity. To avoid large transient motions that would result from an initial state greatly out of equilibrium, we choose the velocity field

$$u_k = +\omega_x y_k, \qquad v_k = -\omega_y x_k \tag{28}$$

where the constants ω_x and ω_y are obtained by substitution of (28) into (6) and (7), together with $\partial/\partial t = 0$, $p_2 = 0$ and $h_1 = 1 - (x/a)^2 - (y/b)^2$. The initial lower layer potential vorticity q_2 is simply a grided sample of a given analytical function ($= 0$ in most experiments, which by the way does not necessarily imply $p_2 = 0$ and an inactive lower layer).

In all runs, we use $N = 5000$ particles per vortex and a 60×60 square grid, on which we impose doubly periodic boundary conditions. Updating of positions and velocities is performed with an Adams–Bashforth scheme [13]. The time step is chosen so that, at every time step, no particle is moved over a distance greater than one-tenth of the grid size. Plots are produced at regular time intervals to display particle positions, contours of upper layer thickness and contours of lower layer potential vorticity (if non-zero).

4.1. Circular vortices

In this first series of experiments we test our model when a single circular vortex sits over a motionless lower layer. A straightforward analytical solution of the governing equations yields the following steady state:

$$u_1 = +\frac{a - \sqrt{a^2 - 8}}{2a}\, y, \qquad v_1 = -\frac{a - \sqrt{a^2 - 8}}{2a}\, x \quad (a > \sqrt{8}) \tag{29a}$$

$$h_1 = p_1 = 1 - \frac{x^2 + y^2}{a^2} \tag{29b}$$

$$p_2 = 0, \qquad q_2 = \delta\left(1 - \frac{x^2 + y^2}{a^2}\right) \tag{29c}$$

inside the circle $x^2 + y^2 = a^2$, and $h_1 = p_2 = q_2 = 0$ outside it. Although the Eulerian solution is unchanging with time, the vortical fluid motion makes the fluid particles go around in circles, and in our PIC model particles move from cell to cell. The test then consists in evaluating the deterioration affecting a flow field that ideally should not change over time.

The dimensionless parameters controlling this set of experiments are the vortex size factor a (ratio of actual radius to the length scale L), the depth ratio δ introduced earlier, the number of cells covering the vortex, and the initial number of particles per cell. Figure 4 shows the deterioration of the upper layer thickness distribution of an insufficiently resolved circular vortex. In this run, the number of particles per cell was only four. Increasing the number of particles gradually improves the situation, and, when we use 15 or more particles per cell, the vortex faithfully preserves its characteristics over time (not shown since all plots are nearly identical). When the average number of particles per cell falls below 15, more but smaller particles are necessary. Conversely, if there are more than 15 particles per cell in average, there is a relative excess of particles for the existing grid, and the mesh can be refined until the average number of particles per cell falls to 15.

Figure 5 traces the evolution of ideal invariants during a relatively long evolution (in excess of four complete revolutions of the vortex), showing how well properties are conserved over time. There are small oscillations, which may be numerical manifestations of so-called inertial oscillations [9], probably due to our initialization, which does not strictly conform to the steady state, but these are not completely understood at this time. It is certain, however, that they do not depend on the number of particles per cell.

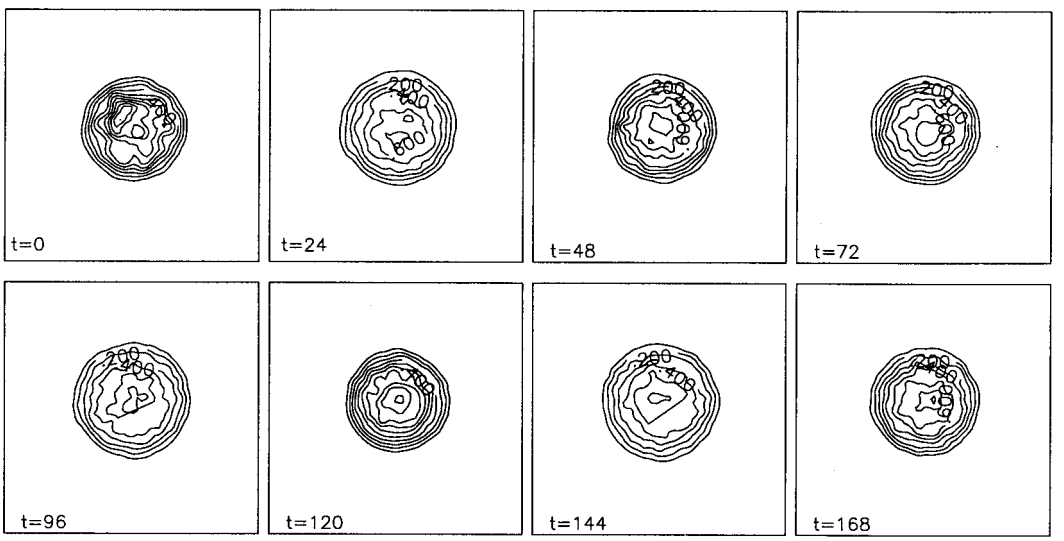

Figure 4. Simulation of a circular vortex ($a = 5.0$, $\delta = 0.25$), showing deterioration because of insufficient number of particles per cell. The initial number of particles per $\Delta \times \Delta$ cell is four.

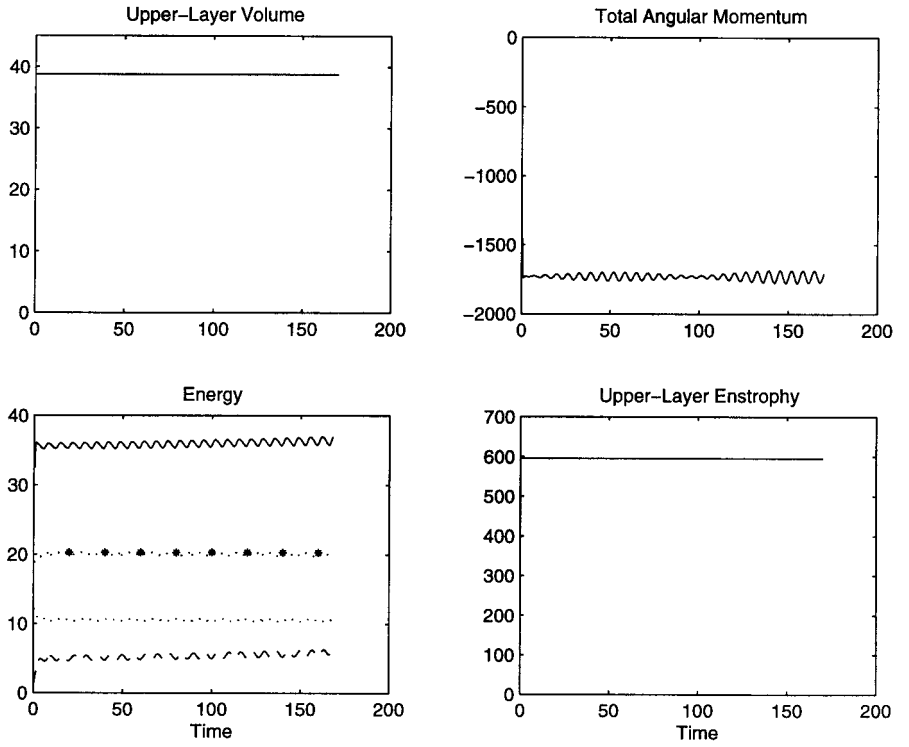

Figure 5. Time series of upper layer volume, total angular momentum, total energy, and upper layer potential vorticity ($m = 1$) for a well-resolved run with a circular vortex ($a = 5.0$, $\delta = 0.25$). In the energy panel, the solid line represents the total energy, the dashed line the upper layer kinetic energy, the dot-star line the lower layer kinetic energy, and the dotted curve the available potential energy of the interfacial displacement. (Oscillations are presumed manifestations of well-resolved inertial oscillations in response to an imperfectly initialized flow field. Curves look jagged only because of the coarse temporal sampling of the invariants.)

Overall, we conclude that the accuracy of the method is assured when the number of particles per cell is about 15, and that the method does not exhibit signs of numerical dissipation.

4.2. Elliptical vortices

We now test our model with a single elliptical vortex. Existing theories [15,16] show that elliptical vortices of the shallow-water equations are stable only up to a critical elongation ratio of $\sqrt{7/2} = 1.87$. Thus, elliptical vortices that have an initial aspect ratio greater than this threshold value naturally tend to seek a stable configuration by reducing their eccentricity.

To initialize an elliptical vortex, we begin again with a circular vortex of unit radius and center depth, but we now stretch the (x_k, y_k) co-ordinates of every particle by different

amounts, namely x_k by a and y_k by b, with $b < a$. The center depth remains unity ($h_0 = 1$), and the volumes are all multiplied by ab. The lower layer potential vorticity is set to zero everywhere ($q_2 = 0$).

Figure 6 presents a typical run with an elliptical vortex. The parameter values are $a = 3.5\sqrt{3} = 6.06$, $b = 3.5/\sqrt{3} = 2.02$, $\delta = 0.25$. The aspect ratio is thus $a/b = 3$, placing the vortex in the unstable range. The sequence of events consists in some expulsion of particles from each tip (a process called filamentation in oceanography), the formation of small satellite vortices from these filaments, the rotation of the remaining vortex core, and its progressive stabilization at a reduced aspect ratio (1.79 ± 0.07 during $128 \leq t \leq 224$). Also worth noting on Figure 6 is how sharp the front (= envelope of particles) remains throughout the simulation and how steady is the rotation of the vortex after its eccentricity reduction. Finally, there is no sign of 'multi-streaming', the documented [17] numerical problem whereby particles that are close to each other travel at significantly different velocities).

An indirect way of assessing the realism of the calculations is to compare the rate of clockwise rotation of the less elongated, final vortex with a theoretical estimate, although the latter was obtained [18] under the limit of very large vortices ($a, b \gg 1$) and deep water ($\delta \ll 1$). Using the dimensions of the final vortex in the theoretical estimate, we infer a (dimensionless) clockwise rotation rate of 0.065 ± 0.008, while the clockwise rotation rate noted from $t = 96$ to $t = 192$ on Figure 6(b) is 0.089. We find this disagreement not unreasonable, especially considering that the theoretical estimate is in this case only a crude approximation.

4.3. Vortex mergers

Next, we present a series of simulations during which two initially distinct vortices interact and eventually merge to form a single, larger vortex. Here, the investigation consists of testing how well the invariants of motions are conserved during a highly complex situation. We now initialize the system with two identical circular vortices of radius a and of unit center depth ($h_0 = 1$), placed apart from each other with distance d between their centers. The lower layer potential vorticity is again set to zero everywhere ($q_2 = 0$).

Figure 7 shows the particle distribution and the upper layer thickness h_1, as time unfolds, whereas Figure 8 traces the evolution of the 'invariants' during the same simulation. It is remarkable how well the invariants are conserved given the substantial changes undergone by the system during the merging process and the following adjustment.

4.4. Vertical interaction of vortices

In a last set of experiments with vortices, we introduce a potential vorticity anomaly in the lower layer ($q_2 \neq 0$) in order to explore the behavior of a structure with vorticity in both upper and lower layers. No analytical theory exists against which we could compare our numerical results, and we therefore present these simulations solely as an illustration of a further type of application of the PIC method.

We initialize the system with an upper layer circular lens floating above, and slightly to the side of, a lower layer disk of non-zero potential vorticity. Without loss of generality, we set the center depth of the lens to unity, and to minimize the number of parameters, we take the disk's potential vorticity as $q_2 = \pm 1$, assign the same radius a to both upper layer lens and lower

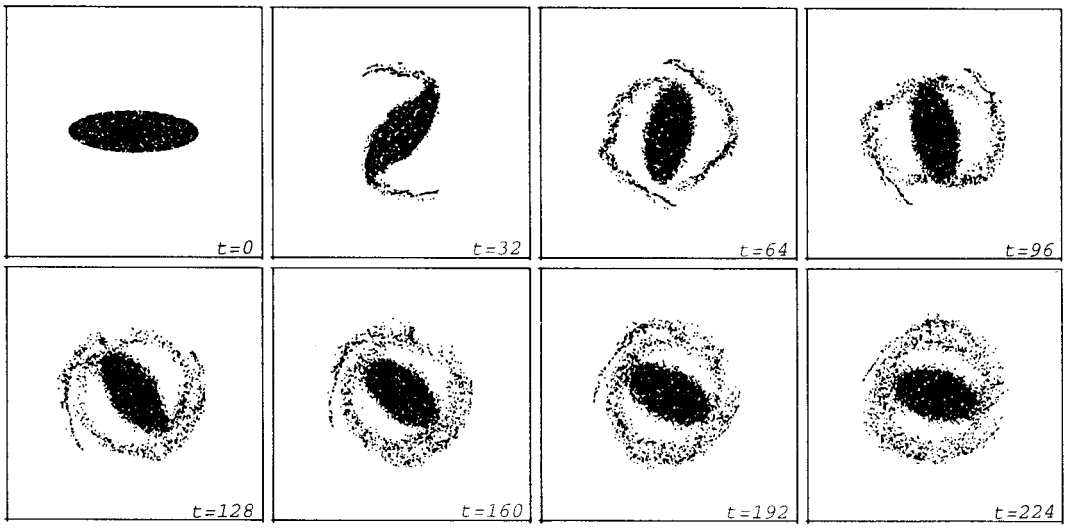

(a)

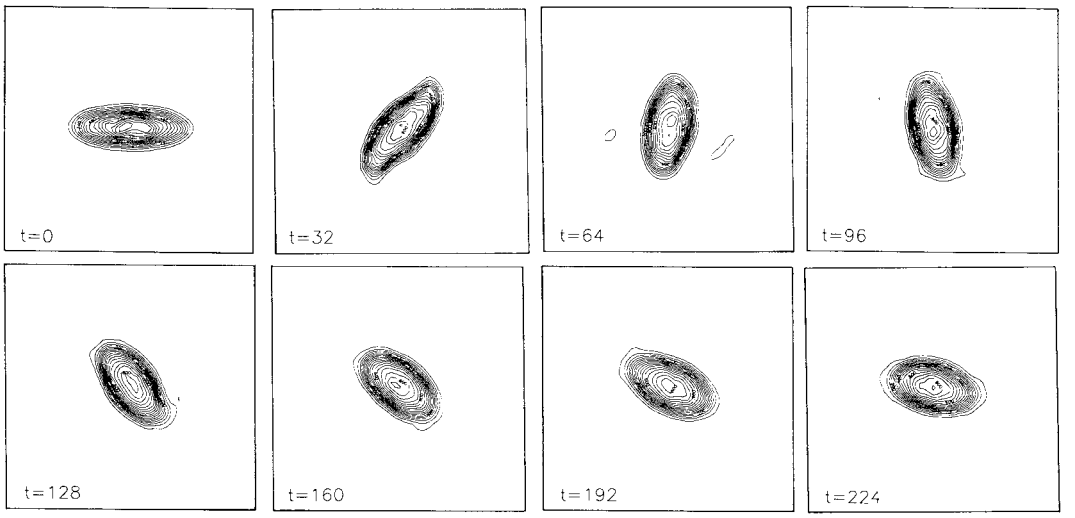

(b)

Figure 6. Simulation of an elliptical vortex undergoing eccentricity reduction ($a = 3.5\sqrt{3} = 6.06$, $b = 3.5/\sqrt{3} = 2.02$, $\delta = 0.25$ and $q_2 = 0$): (a) particle positions, and (b) h_1 contours. Note how well defined the front (= envelope of particles) remains at all times despite the substantial changes undergone by the vortex and the filaments it produces.

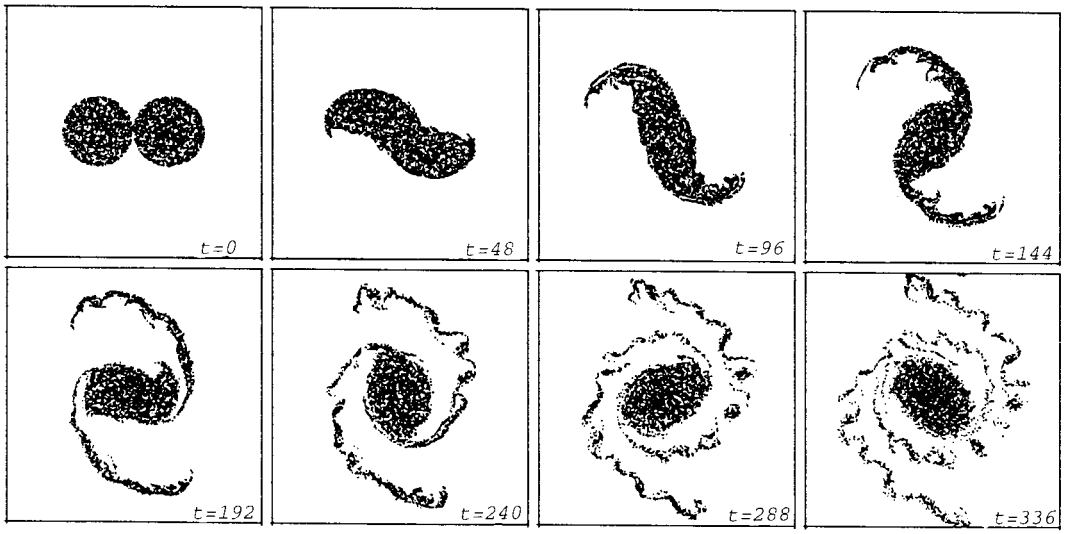

(a)

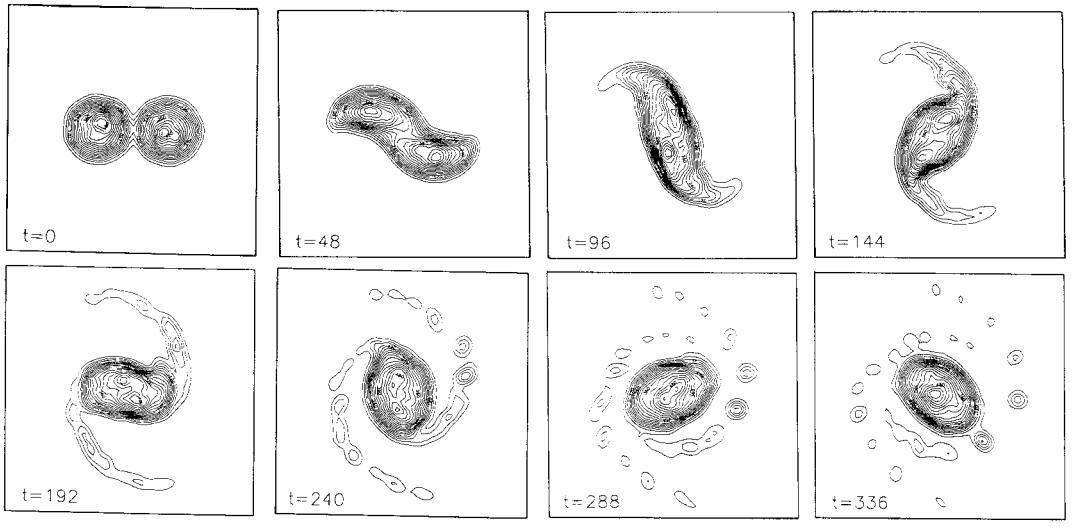

(b)

Figure 7. Simulation of a vortex merger ($a = b = 5.0$, $\delta = 0.25$ and $q_2 = 0$): (a) particle positions and (b) h_1 contours.

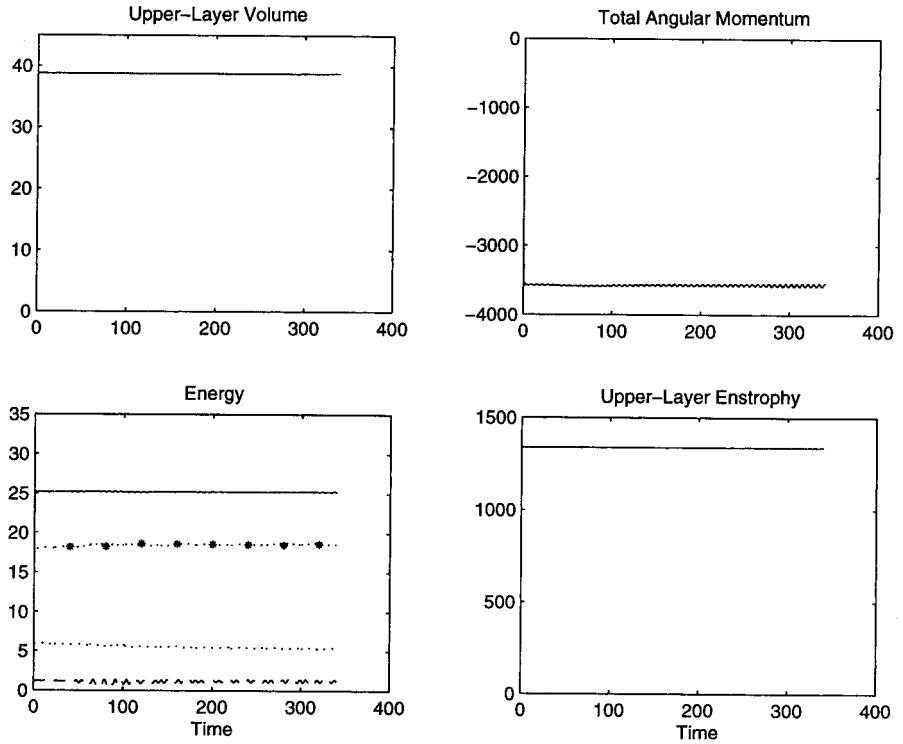

Figure 8. Time series of the 'invariants' during the simulation depicted in Figure 7. In the energy panel, the solid line corresponds to the total energy, the dashed line to the lower layer kinetic energy, the dot-star line to the lower layer kinetic energy, and the dotted line to the available potential energy of the interfacial displacements.

layer disk, and choose a separation distance between centers of $a/2$. (A non-zero separation distance is necessary to create an unsteady situation.)

Figure 9 traces the evolution of the upper layer particles and lower layer pressure distribution when parameter values are $q_2 = +1$, $a = 3.5$ and $\delta = 0.25$. From the sequence of plots, we notice that the two vortices distort somewhat to adjust to each other's lateral presence, yet retain their integrity. Also, because of their individual rotation, they entrain each other along a curved path (with a common center of rotation lying outside of their individual centers). A similar behavior was obtained in a theoretical study [11] with much simpler dynamics (point vortices and very weak vertical displacement of the density interface between the two layers, and therefore no outcropping).

Figure 10 shows a different situation when q_2 is set to -1 (upper and lower vortices then have identical polarities, both rotating clockwise). In this case, the two vortices again adjust to each other's presence but now rotate around each other (with their common center of rotation lying between their individual centers).

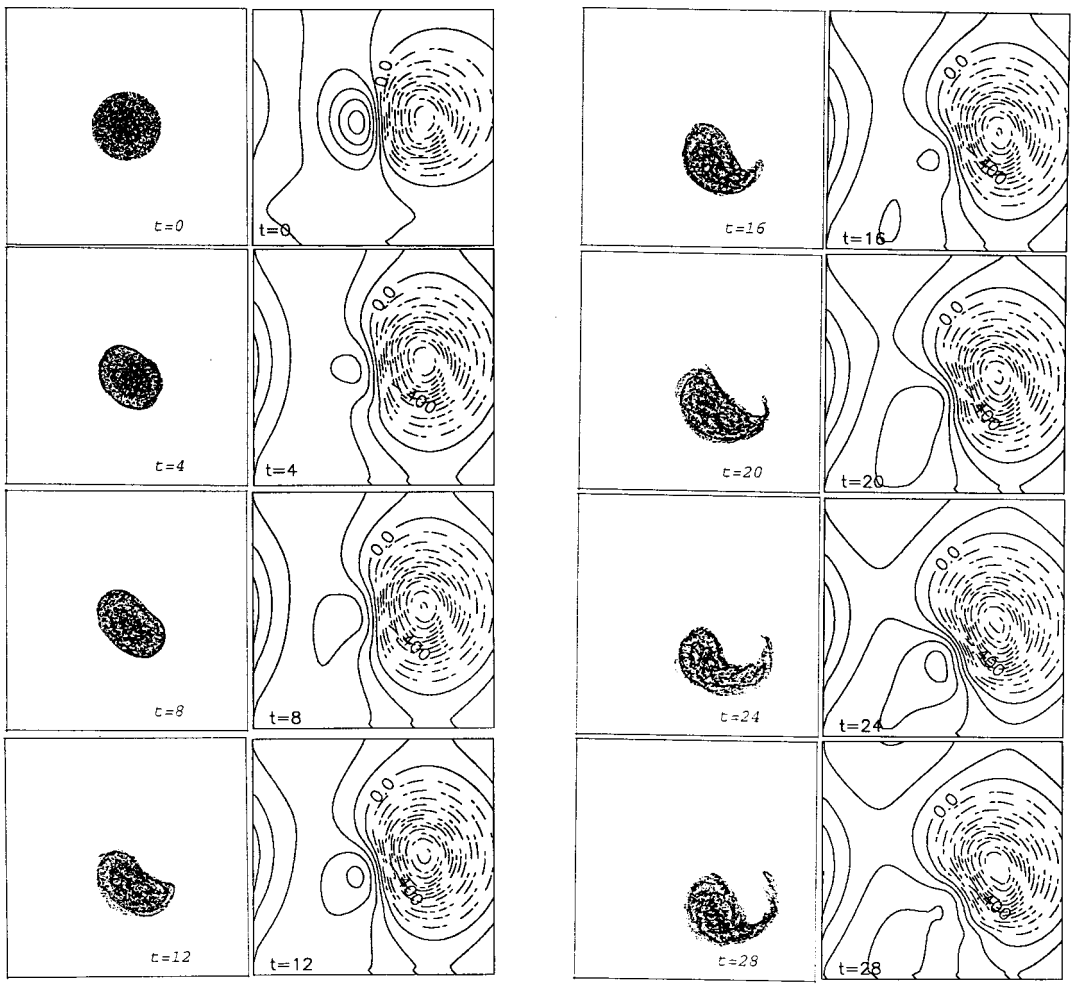

Figure 9. Simulation of a double structure consisting of an upper layer circular lens floating above, and slightly to the side of, a lower layer circular anomaly of potential vorticity ($q_2 = +1$): (a) upper layer particles, (b) lower layer pressure distribution.

5. IMPLEMENTATION OF A LATERAL RIGID BOUNDARY

While the PIC method is ideally suited for distorting fronts, it faces difficulties in the presence of rigid boundaries. In a traditional, Eulerian-based method, it is straightforward to put to

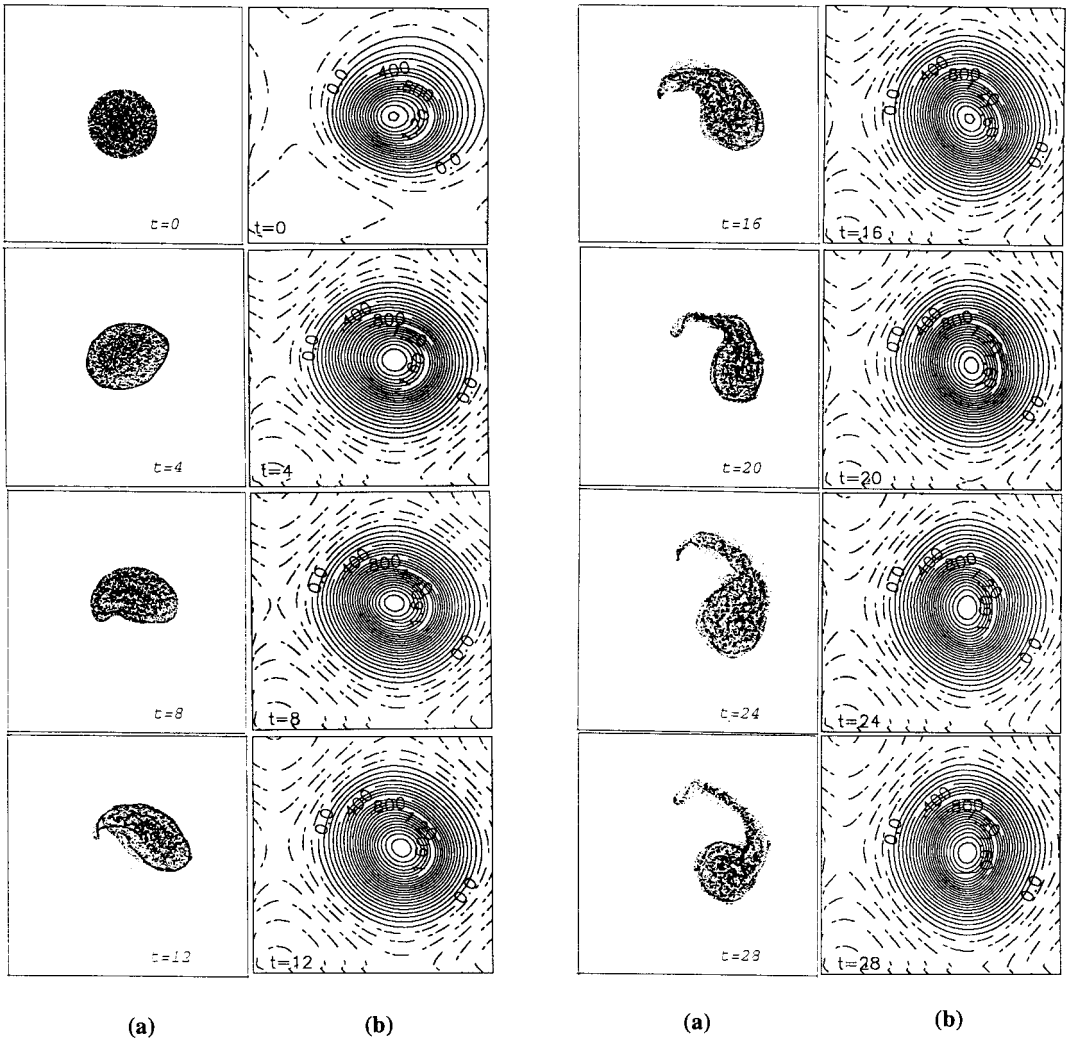

Figure 10. Similar simulation, but with $q_2 = -1$: (a) upper layer particles, (b) lower layer pressure distribution.

zero the velocity component normal to a boundary, but in the Lagrangian-based PIC method, where the velocities are updated from accelerations, this cannot be done simply. The presence of a rigid boundary must somehow be communicated to the approaching particles, and this demands a careful consideration of the interaction between one particle and the boundary.

To overcome the difficulty, we apply a simple-minded reflection scheme [19]. In this scheme, whenever a particle hits the boundary it is simply reflected like a billiard ball. Caution, however, must be exercised in dealing with finite time stepping in the presence of the Coriolis force. The x and y momentum equations (23) and (24) for particle k near the wall can be written in dimensional form as

$$\frac{\mathrm{d}}{\mathrm{d}t}(u_k - fy_k) = \text{pressure force in the } x\text{-direction} \tag{30a}$$

$$\frac{\mathrm{d}}{\mathrm{d}t}(v_k - fx_k) = \text{pressure force in the } y\text{-direction} \tag{30b}$$

Now let us consider the impact of that particle on a wall situated at $x = 0$. Should x_k become negative at the next time step, we use mirror symmetry and impose

$$x_k^{\text{new}} = -x_k^{\text{old}}, \qquad y_k^{\text{new}} = +y_k^{\text{old}} \tag{31}$$

As our system is frictionless, no force acts in the direction tangential to the wall, so the y component of momentum of the particle must be conserved. By integrating this momentum equation (30b) from the moment immediately preceding the collision of the particle on the wall to the instant of time immediately after the collision, we obtain

$$\Delta(v_k + fx_k) = \text{impulse in } y = 0 \tag{32}$$

where Δ indicates the difference occurring during reflection. This constraint yields

$$v_k^{\text{new}} = v_k^{\text{old}} + f(x_k^{\text{old}} - x_k^{\text{new}}) = v_k^{\text{old}} + 2fx_k^{\text{old}} \tag{33}$$

A different result would have been obtained if we had used a simple reflection approach ($v_k^{\text{new}} = v_k^{\text{old}}$), as it has been proposed earlier [20]. Note that, in the limit of an infinitesimally small time step, x_k^{old} tends to zero and the difference between the two schemes vanishes.

Similar considerations for particles near the other boundary at $x = D$ lead to the following scheme: would a particle move beyond the domain, i.e. $x_k^{\text{old}} > D$, then $x_k^{\text{new}} = 2D - x_k^{\text{old}}$, $y_k^{\text{new}} = y_k^{\text{old}}$, and $v_k^{\text{new}} = v_k^{\text{old}} + 2f(x_k^{\text{old}} - D)$. Finally, because our code uses dimensionless variables, the Coriolis parameter f is set to unity.

Using this algorithm, we ensure conservation of the tangential momentum of particles interacting with the wall. The component of momentum perpendicular to the wall is not conserved because of the non-zero impulse exerted by the wall in reflecting the particle. If we merely reverse the sign of u_k (i.e. $u_k^{\text{new}} = -u_k^{\text{old}}$), the kinetic energy of the particle striking the wall is not conserved, although it should be. We enforce conservation of energy by applying a factor to the x component of velocity, by writing

$$u_k^{\text{new}} = -\sigma u_k^{\text{old}} \tag{34a}$$

where the factor σ is such that $(u_k^{\text{new}})^2 + (v_k^{\text{new}})^2 = (u_k^{\text{old}})^2 + (v_k^{\text{old}})^2$, wherefrom

$$\sigma = \sqrt{1 + \frac{(v_k^{\text{old}})^2 - (v_k^{\text{new}})^2}{(u_k^{\text{old}})^2}} \tag{34b}$$

In all our calculations, this factor differs only slightly from unity.

6. COASTAL CURRENT SIMULATIONS

Our present interest is in discerning the possible outcomes under varying parameters (current width, frontal strength, etc.). Because we are not interested in the behavior of the nose of a coastal intrusion and we do not consider how a flow, like a river runoff, turns toward the coast and is held against it by the Coriolis force, we assume that our coastal current pre-exists and occupies the entire, straight coastline; for this, it must be in so-called geostrophic balance (equilibrium between the Coriolis force and pressure gradient force: $-v_1 = -\partial p_1/\partial x$, $+u_1 = 0$).

The domain consists of a channel bounded in the x-direction by parallel walls (at $x = 0$ and D) and with periodicity in the y-direction. We use a 60×120 spatial grid with $N = 12000$ or more particles. To initialize the flow, particles are first randomly and uniformly distributed over an area $a \times b$ (where a is the width of the current against the left wall, and b is the length of the domain in the y-direction), according to

$$x_k = an_1, \qquad y_k = bn_2 \tag{35}$$

where (n_1, n_2) is the kth pair in a series of random numbers between 0 and 1. For all our runs, we take $b = 12a$.

Because of their random positioning, all particles have the same cross-sectional area, equal to ab/N. Then, each particle is assigned a volume depending on its position and the desired profile of the upper layer thickness. In all of the experiments we use a parabolic profile $h_1(x) = 1 - x^2/a^2$, which vanishes at the offshore front ($x = a$) and reaches a maximum at the wall ($x = 0$). This maximum value is unity by virtue of the non-dimensionalization of the equations. Therefore, the volume V_k of particle k is

$$V_k = \left(1 - \frac{x_k^2}{a^2}\right)\frac{ab}{N} \tag{36}$$

We then assign initial velocity components to every particle, by requiring that the current be initially steady (in the so-called geostrophic equilibrium)

$$u_k = 0, \qquad v_k = \left.\frac{\partial p_1}{\partial x}\right|_k \tag{37}$$

However, because $p_1 = p_2 + h_1$, we first need to calculate the initial pressure field in the lower layer, using Equation (9). Taking a uniform potential vorticity in the lower layer [$q_2(t=0)=0$], we seek a solution to the equation

$$\nabla^2 p_2 = -\delta h_1 \tag{38}$$

Integrating twice with respect to x and using boundary conditions ($p_2 = 0$, $\mathrm{d}p_2/\mathrm{d}x = 0$ at $x = a$), we obtain

$$p_2 = \delta\left(\frac{x^4}{12a^2} - \frac{x^2}{2} + \frac{2ax}{3} - \frac{a^2}{4}\right) \tag{39}$$

Using this expression for p_2, we can finally determine p_1 from $p_1 = p_2 + h_1$ and derive the particle velocities from (37)

$$v_k = -\frac{2x_k}{a^2} + \delta\left(\frac{x_k^3}{3a^2} - x_k + \frac{2a}{3}\right) \tag{40}$$

Currents in our numerical experiments can be characterized by their geometric structure, i.e. width (non-dimensionalized as a) and maximum coastal depth (hidden in the definition of δ). Because observations reveal that the majority of coastal currents fall in this range of parameters, we performed our experiments with dimensionless widths a ranging between 1.9 and 60, and with a depth ratios δ of 0.1 and 0.2.

We start with a current that is wide ($a = 60$) and shallow ($\delta = 0.1$). These parameters lead to a stable flow (not shown), which preserves its shape for the entire time of our experiment (910 time units, or 144 inertial oscillations). The flow is rather slow, and the existing horizontal shear is not sufficient for any instability to become noticeable.

We then decrease the current width successively to $a = 19$, 6.0 and 1.9. (Because of our scaling, this trend is physically analogous to increasing the coastal depth under fixed width.) As Figures 11–13 show, the current becomes increasingly wavy and unstable. Simulations with a larger value of δ ($\delta = 0.2$, *viz.* a lower layer half as deep) were also performed but did not show qualitative differences. A physical interpretation of the frontal waves and of their finite amplitude growth lies beyond the scope of this article (and of this journal). It suffices to say that in a companion paper [21] we discuss those matters and find good agreement with data reported from laboratory experiments and oceanographic observations. There are no numerical simulations available for comparison because the present calculations are the first ever numerical simulations of a two-layer coastal current with outcropping density interface on its offshore flank.

7. CONCLUSIONS

We have described a particle-in-cell (PIC) method suitable for geophysical fluid applications to systems with two density layers and outcropping interface. Several tests of the algorithm were

performed, which demonstrated that the method is robust and quite accurate. Since the application of the PIC method to geophysical fluids, especially those with stratification, is still in its infancy, refinements can and should be made in the future that would further increase the accuracy of the algorithm. It would also be highly desirable in the future to see modifications that would enable parallel computations. Indeed, as it stands the code uses two independent indexing systems, one for the particles and another for the grid, with no straightforward numerical relationship between the two as particles move across grid cells in the course of

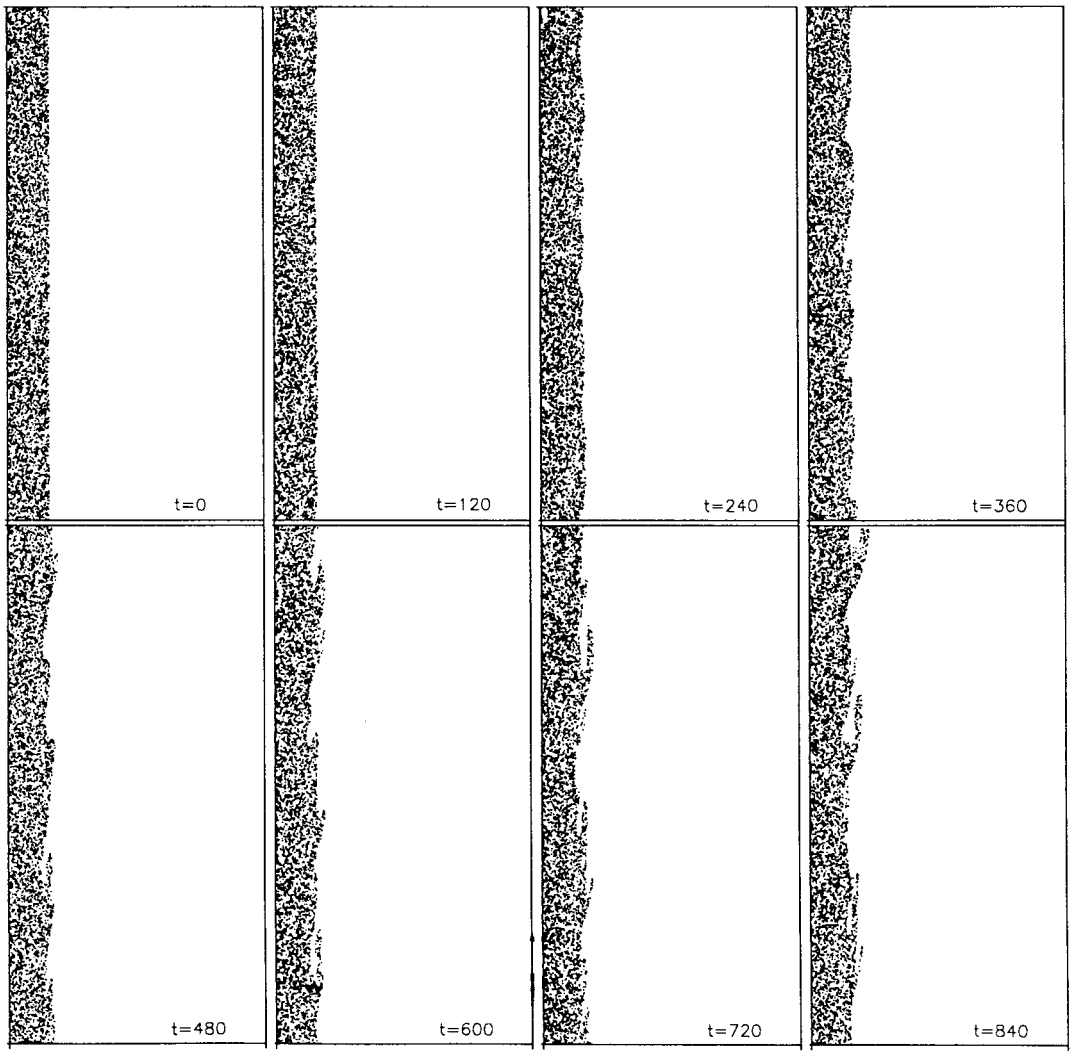

Figure 11. Simulation of a coastal current ($a = 19$).

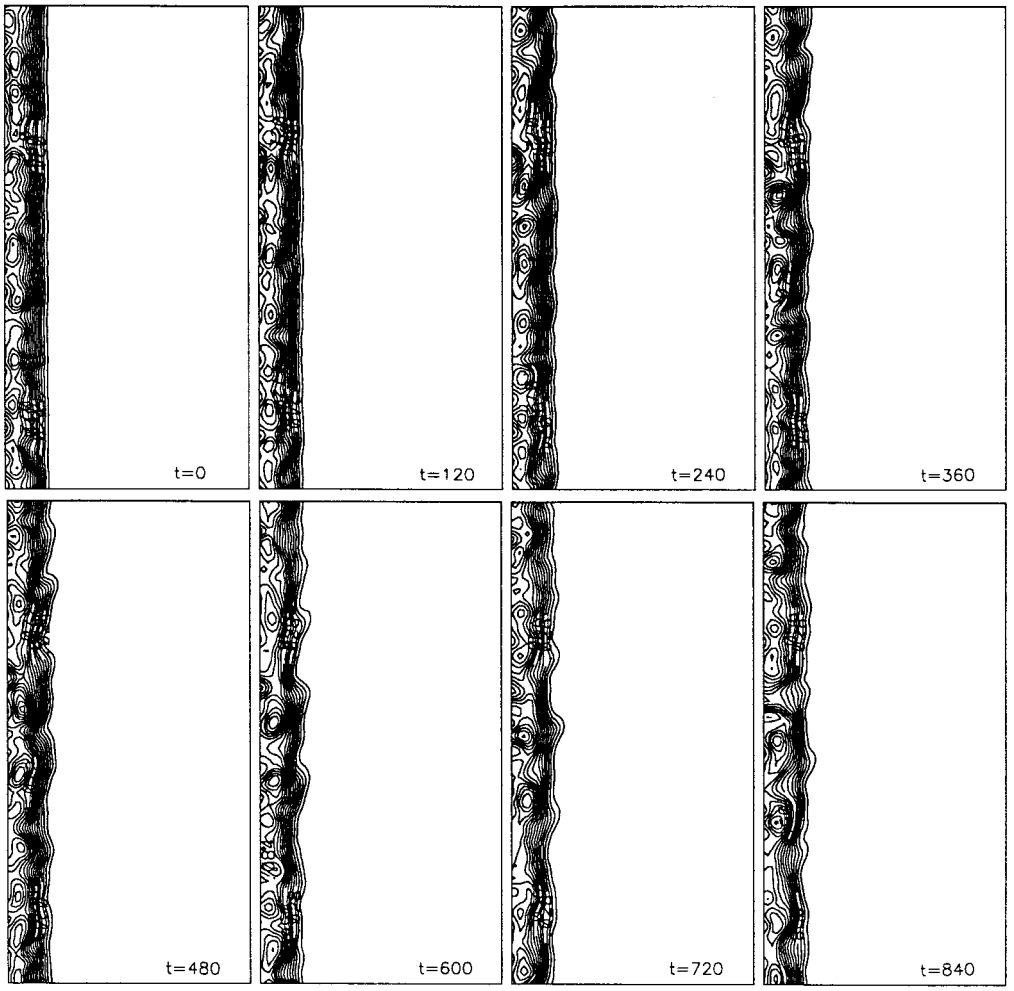

Figure 11 (*Continued*)

integration. Thus, the transfer of information from particle to grid and back several times per time step cannot be performed in a parallel fashion and consumes about 80–85% of the computer's CPU time. Changing this situation would translate into large computational gains (much shorter integration times and/or use of many more particles).

The variety of applications shown here proves the flexibility of the method. Although it is not *a priori* trivial to initialize a set of particles that corresponds to a given initial flow, we have proposed a random assignment procedure that eliminates the problem of determining how closely packed the particles ought to be as a function of space; rather than assigning equal

volumes to all particles and varying their packing with location, we pack the particles uniformly and vary their volume in a simple way according to the Eulerian-posed initial conditions. Besides making the initialization procedure very generic and thus flexible, our method also ensures uniform coverage of the domain (or the relevant parts thereof) by particles, at least for the early moments of integration. Should the particle density become unacceptably low in some areas of the domain after a certain time of integration, the

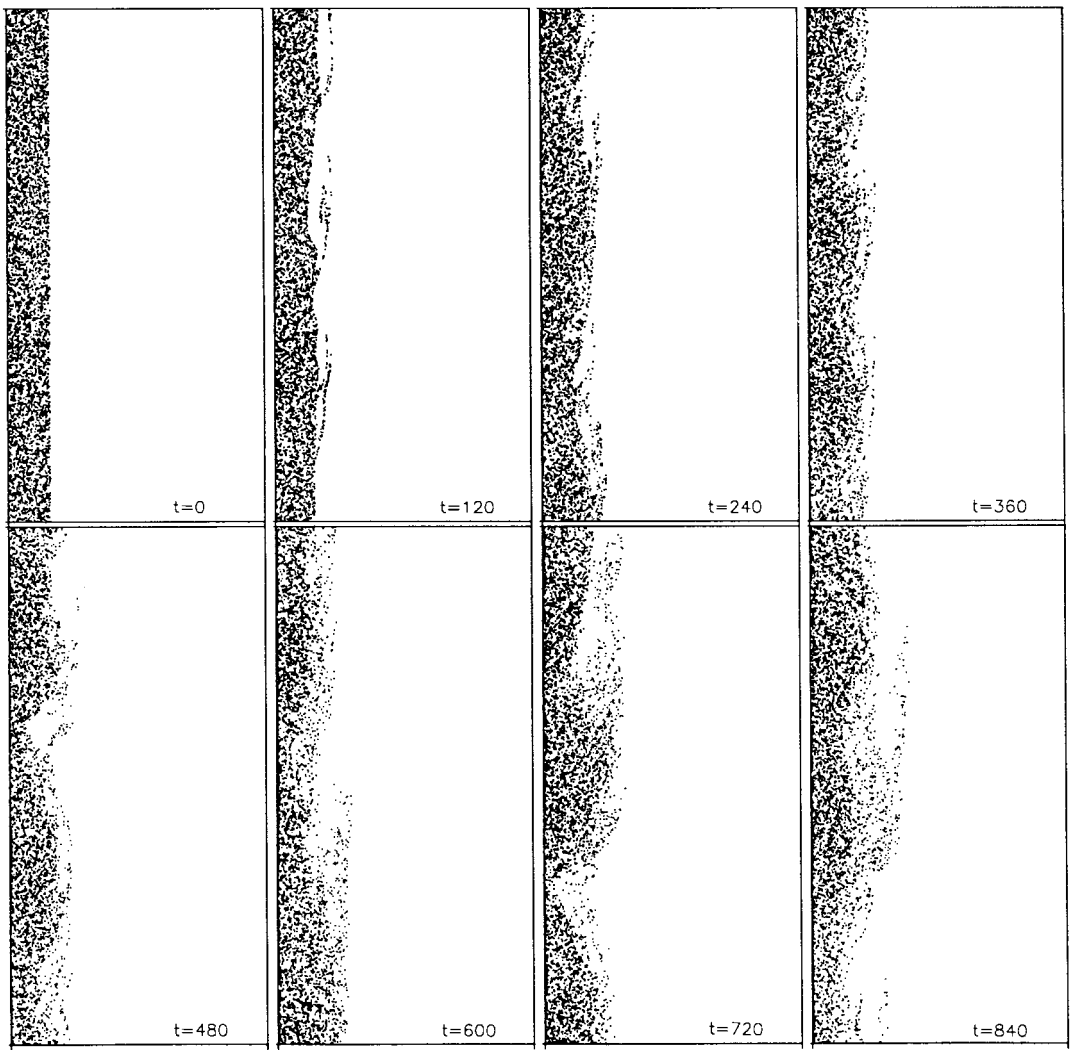

Figure 12. Same as Figure 11, but with a relatively narrower current ($a = 6.0$).

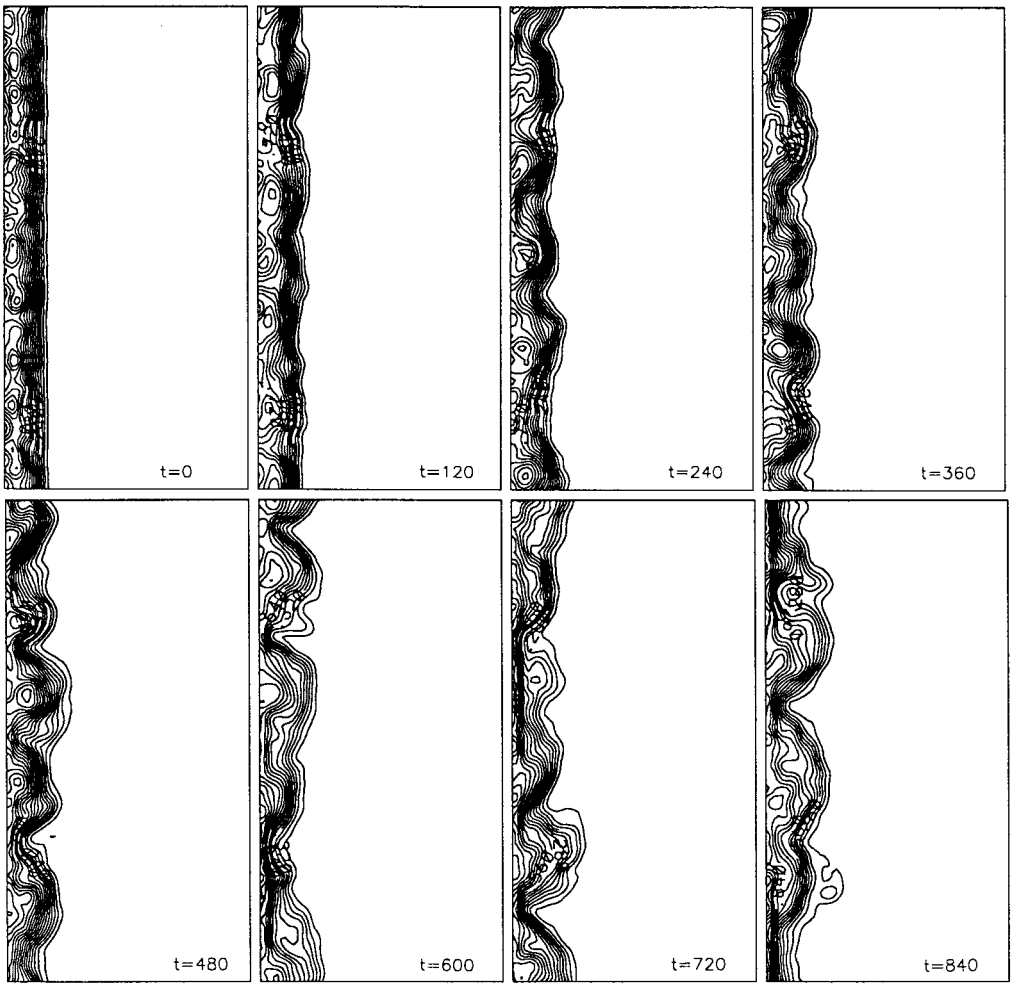

Figure 12 (*Continued*)

creation of a new particle set, either locally or globally, could be straightforwardly designed following the lines of our initialization procedure. Finally, the random aspect of our initialization procedure avoids all together the spurious effects that could result from useless initial symmetries (such as initial particle positions along straight lines or concentric circles).

It should be mentioned in closing that the restriction to two density layers and the use of a rectangular grid are by no means rigid features of the PIC method described here. Generalization to more than two layers is straightforward: treat with Lagrangian particles

all layers of which the thickness vanishes inside the computational domain (at the intersection of two density interfaces or of an interface with either the top or bottom), and treat all layers that exist throughout the domain at all times by a conventional method of integration. Generalizations to non-rectangular cells, such as finite elements, is also possible, although not as straightforward. Such an approach requires a procedure to transfer fractional particle volumes to neighboring nodes in a way compatible with the local mesh.

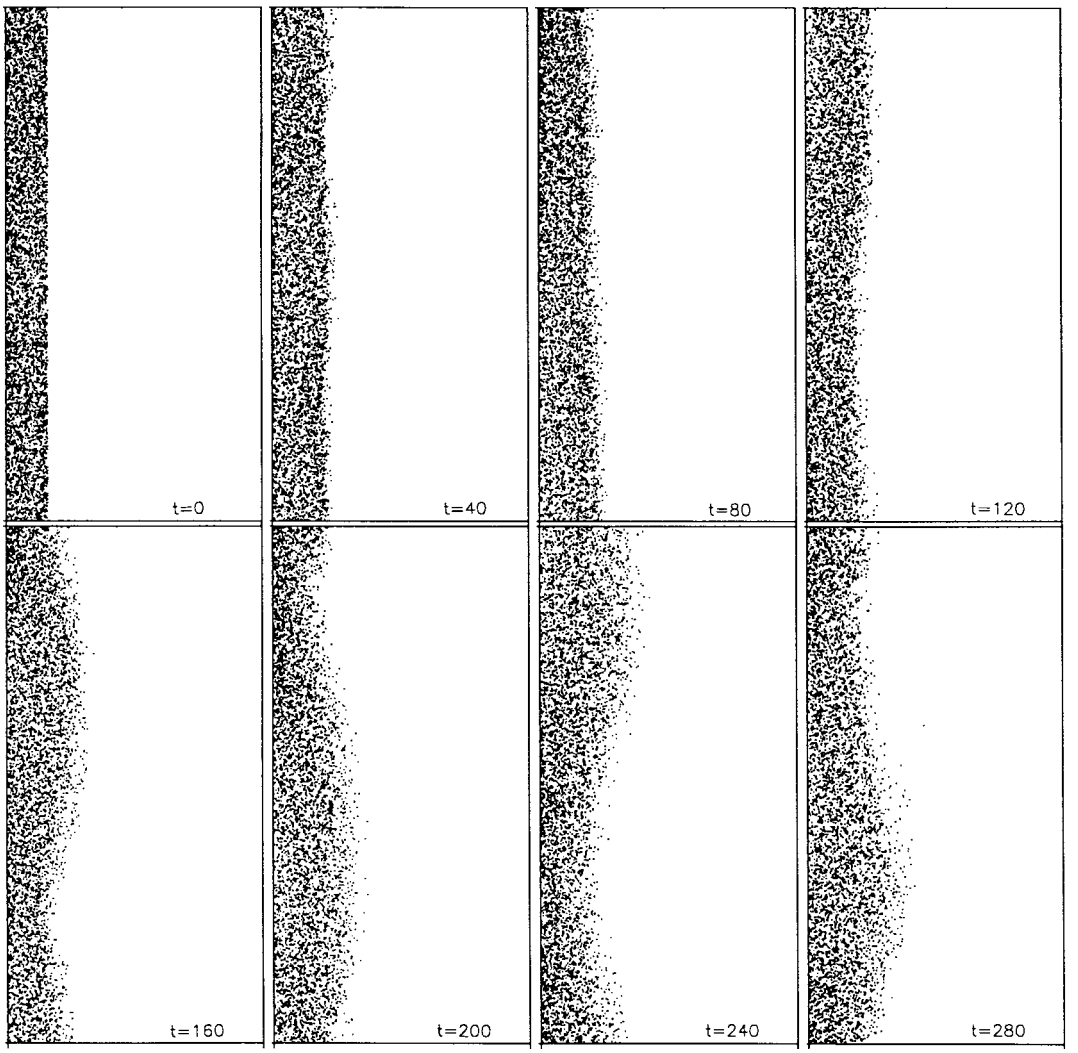

Figure 13. Same as Figures 11 and 12, but with an even narrower current ($a = 1.9$).

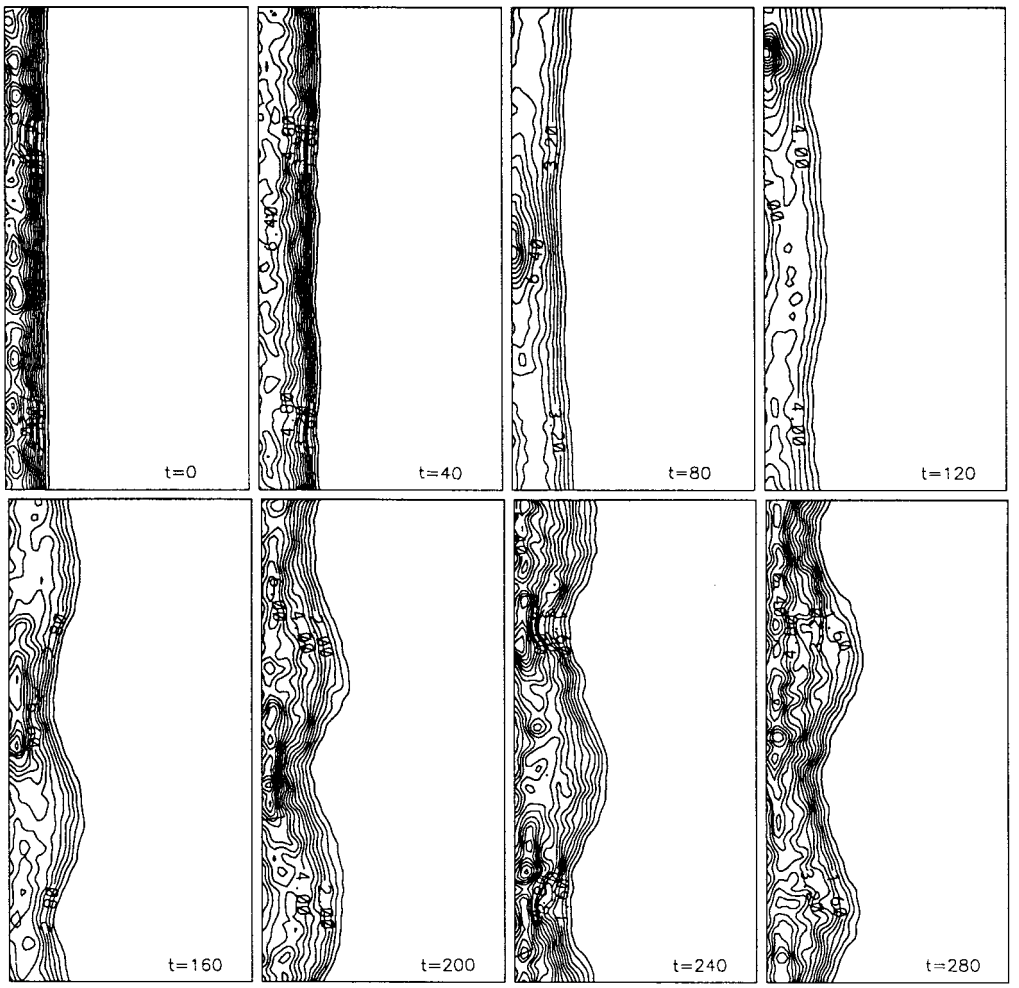

Figure 13 (*Continued*)

ACKNOWLEDGMENTS

This research was made possible by grants of the Office of Naval Research (N0001493-I-0391) and of the National Science Foundation (OCE-9118426) to Dartmouth College, for which the authors express their sincere appreciation. Helpful remarks from numerous colleagues, particularly Dr A. D. Kirwan Jr., are also graciously acknowledged.

REFERENCES

1. Chaudhry MH. *Open-Channel Flow*. Prentice Hall: Englewood Cliffs, NJ, 1993.
2. Hirt CW, Nichols BD, Romero NC. *SOLA—a numerical solution algorithm for transient fluid flows*. Los Alamos Scientific Laboratory Report LA-5852, University of California, 1975.
3. Hirt CW, Nichols BD. Volume of fluid (VOF) method for the dynamics of free boundaries. *Journal of Computational Physics* 1981; **39**: 201–225.
4. Nakayama T, Mori M. An Eulerian finite element method for time-dependent free surface problems in hydrodynamics. *International Journal for Numerical Methods in Fluids* 1996; **22**: 175–194.
5. Brackbill JU, Ruppel HM. FLIP: a method for adaptively zoned, particle-in-cell calculations of fluid flows in two dimensions. *Journal of Computational Physics* 1986; **65**: 314–343.
6. Hockney RW, Eastwood JW. *Computer Simulation Using Particles*. Adam Hilger: Bristol, 1988.
7. Pavia EG. *A numerical study of merging and axisymmetrization of oceanic eddies*. PhD Thesis, Florida State University, 1989.
8. Pavia EG, Cushman-Roisin B. Modeling of oceanic fronts using a particle method. *Journal of Geophysical Research* 1988; **93**: 3554–3562.
9. Pavia EG, Cushman-Roisin B. Merging of frontal eddies. *Journal of Physical Oceanography* 1990; **20**: 791–814.
10. Aref H. Integrable, chaotic, and turbulent vortex motion in two-dimensional flows. *Annual Review of Fluid Mechanics* 1983; **15**: 345–389.
11. Hogg NG, Stommel HM. The heton, an elementary interaction between discrete baroclinic vortices, and its implications concerning eddy heat-flow. *Proceedings of the Royal Society of London A* 1985; **397**: 1–20.
12. Mathias BJ. *Simulations of vortex evolution and interaction in a two-layer ocean with a particle method*. MS Thesis, Dartmouth College, 1992.
13. Schwarz HR. *Numerical Analysis: A Comprehensive Introduction*. Wiley: New York, 1989.
14. Arakawa A, Mesinger F. Numerical methods used in atmospheric models. In *Global Atmospheric Research Program*, *Vol. 1*. GARP Publication Series No. 17, 1976; 1–42.
15. Cushman-Roisin B. Linear stability of large, elliptical warm-core rings. *Journal of Physical Oceanography* 1986; **16**: 1158–1164.
16. Ripa P. On the stability of elliptical vortex solutions of the shallow-water equations. *Journal of Fluid Mechanics* 1987; **183**: 343–363.
17. LeBoeuf JN, Tajima T, Dawson JM. A magnetohydrodynamic particle code for fluid simulation of plasmas. *Journal of Computational Physics* 1979; **31**: 379–408.
18. Cushman-Roisin B, Merchant-Both S. Elliptical warm-core rings in a two-layer ocean with ambient shear. *Journal of Physical Oceanography* 1995; **25**: 2011–2024.
19. Esenkov OE. *Simulations of coastal currents in a two-layer ocean with a particle-in-cell method*. MS Thesis, Dartmouth College, 1994.
20. Sanson LZ, Graef F, Pavia EG. Collision of anticyclonic, lens-like eddies with a meridional western boundary. *Journal of Geophysical Research* 1998; **103**: 24881–24890.
21. Esenkov OE, Cushman-Roisin B. Modeling of two-layer eddies and coastal flows with a particle method. *Journal of Geophysical Research* 1999; **104**: 10959–10980.

